Joint ToF Image Denoising and Registration with a CT Surface in Radiation Therapy

Sebastian Bauer[1], Benjamin Berkels[3], Joachim Hornegger[1,2], Martin Rumpf[4]

[1] Pattern Recognition Lab, Dept. of Computer Science
[2] Erlangen Graduate School in Advanced Optical Technologies (SAOT)
Friedrich-Alexander-Universität Erlangen-Nürnberg,
Martensstr. 3, 91058 Erlangen, Germany
{sebastian.bauer,joachim.hornegger}@informatik.uni-erlangen.de
[3] Interdisciplinary Mathematics Inst., University of South Carolina
Columbia, SC 29208, USA, berkels@mailbox.sc.edu
[4] Inst. for Numerical Simulation, Rheinische Friedrich-Wilhelms-Universität Bonn,
Endenicher Allee 60, 53115 Bonn, Germany, martin.rumpf@ins.uni-bonn.de

Abstract. The management of intra-fractional respiratory motion is becoming increasingly important in radiation therapy. Based on in advance acquired accurate 3D CT data and intra-fractionally recorded noisy time-of-flight (ToF) range data an improved treatment can be achieved. In this paper, a variational approach for the joint registration of the thorax surface extracted from a CT and a ToF image and the denoising of the ToF image is proposed. This enables a robust intra-fractional full torso surface acquisition and deformation tracking to cope with variations in patient pose and respiratory motion. Thereby, the aim is to improve radiotherapy for patients with thoracic, abdominal and pelvic tumors. The approach combines a Huber norm type regularization of the ToF data and a geometrically consistent treatment of the shape mismatch. The algorithm is tested and validated on synthetic and real ToF/CT data and then evaluated on real ToF data and 4D CT phantom experiments.

1 Introduction

In this paper, we propose a variational framework that simultaneously solves denoising of time-of-flight (ToF) range data and its registration to a surface extracted from computed tomography (CT) data. Thereby, we underline the benefits of such a joint variational approach. As a case study we show its potential for improvements in radiation therapy planning and treatment. Our algorithm is tested on synthetic and real ToF/CT data using a rigid torso phantom with real ToF data and a 4D CT phantom. We show that the method is capable to cope both with deformations caused by a variation in the patient positioning and by the respiratory motion.

Compensation of Respiratory Motion as a Challenge in Radiation Therapy. The management of respiratory motion in diagnostic imaging, interventional imaging

and therapeutic applications is an evolving field with many current and future issues still to be adequately addressed. In particular, effects due to organ and tumor motion attract considerable attention in radiation oncology [1]. Technologies that allow an increased dose to the tumor while sparing healthy tissue will improve the balance between complication and cure. Besides a typical patient setup error of 3-5 mm (1 standard deviation) with thoracic radiotherapy [2], a fundamental source of error and uncertainties in radiation therapy is caused by respiratory motion during delivery. Thus, real-time tumor-tracking methods based on the proper identification of thorax deformations due to breathing will significantly improve the radiation therapy. Recently, it has been demonstrated that respiratory motion can be effectively monitored using real-time 3D surface imaging [3]. Schaller et al. [4] presented a time-of-flight respiratory motion detection system that estimates at the ToF frame rate of 25 fps two 1D-signals for the thorax and abdomen movement, respectively. Fayad et al. [5] proposed to use ToF as surrogate to develop a respiration model using PCA. In [6, 7] a patient specific respiration model for use in radiotherapy has been investigated.

Time-of-Flight Imaging. ToF imaging directly acquires 3D metric surface information with a single sensor based on the phase shift ρ between an actively emitted and the reflected optical signal [8]. Based on ρ, the radial distance (range) r from the sensor element to the object can be computed as $r = \frac{c\rho}{4\pi f_{mod}}$ where f_{mod} denotes the modulation frequency and c the speed of light. The technology has recently been proposed for diagnostic, interventional and therapeutic medical applications such as patient positioning [9] and respiratory motion detection [4]. However, due to physical limitations of the sensor, depth data from ToF cameras are subject to high temporal noise and exhibit systematic errors. Temporal noise is usually reduced by temporal averaging and can be further smoothed by employing edge preserving filters [10].

Joint Variational Methods in Imaging. Given a pre-fractionally acquired CT image and an intra-fractionally recorded sequence of ToF images of a torso we set up a variational approach, which combines the two highly intertwined tasks of denoising the ToF image and registration of the ToF surface of the thorax with the corresponding surface extracted from the CT data. Indeed, tackling each task would benefit significantly from prior knowledge of the solution of the other tasks. Joint variational methods have proven to be powerful approaches in imaging. E.g. already in 2001 Yezzi, Zöllei and Kapur [11] and Unal et al. [12] have combined segmentation and registration and Feron and Mohammad-Djafari [13] proposed a Bayesian approach for the joint segmentation and fusion of images. Droske and Rumpf proposed in [14] a variational scheme for morphological image denoising and registration based on nonlinear elastic functionals. Recently, in [15] Buades et al. proposed sharpening methods for images, based on joint denoising and matching of images taken as an image burst.

The paper is organized as follows. In Section 2, we introduce the model for joint registration and denoising, including the functional definitions and variational formulations, while Section 3 covers the numerical implementations. In

Section 4, we study the parameter setting of the method and show experimental results. Eventually, we draw a conclusion in Section 5.

2 A Joint Registration and Denoising Approach

In this section, we will describe the underlying geometric configuration, derive the variational model and prove the existence of minimizers.

Geometric Configuration

Let us assume that we have already extracted a reliable surface $\mathcal{G}_{\mathrm{CT}} \subset \mathbb{R}^3$ from the given CT image. Now, given the ToF camera parameters, we denote by $\mathcal{G}_r$ the corresponding (unknown) noise free surface geometry uniquely described by the range data (ToF) r. Indeed, for each point ξ on the image plane Ω a range value $r(\xi)$ describes a position vector $X_r(\xi) \in \mathbb{R}^3$ with

$$X_r(\xi) = r(\xi)\gamma(\xi)\,,$$

where the transformation $\gamma : \Omega \to S^2$; $\gamma(\xi) = \left(|\xi|^2 + d_f^2\right)^{-\frac{1}{2}} (\xi_1, \xi_2, d_f)$ is based on the pinhole camera model with d_f denoting the focal length. Now, the pre-fractionally acquired surface $\mathcal{G}_{\mathrm{CT}}$ differs from the intra-fractionally found surface $\mathcal{G}_r$ (cf. Fig. 1).

In our application scenario, the shape of $\mathcal{G}_r$ depends on the actual positioning of the patient on the therapy table and the current state of the respiratory motion at the acquisition time of the ToF image. Hence, we consider a deformation ϕ matching $\mathcal{G}_r$ and $\mathcal{G}_{\mathrm{CT}}$ in the sense that $\phi(\mathcal{G}_r) \subset \mathcal{G}_{\mathrm{CT}}$ and that this deformation can best be represented by a displacement u defined on the parameter domain Ω with

$$\phi(X_r(\xi)) = X_r(\xi) + u(\xi)\,.$$

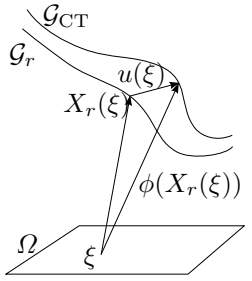

Fig. 1. A geometric sketch of the registration configuration.

To quantify the closeness of $\phi(\mathcal{G}_r)$ to $\mathcal{G}_{\mathrm{CT}}$ we represent $\mathcal{G}_{\mathrm{CT}}$ by the corresponding signed distance function d with $d(x) := \pm\mathrm{dist}(x, \mathcal{G}_{\mathrm{CT}})$, where the sign is positive outside the object domain bounded by $\mathcal{G}_{\mathrm{CT}}$ and negative inside. In particular $d = 0$ on $\mathcal{G}_{\mathrm{CT}}$. Furthermore, $|\nabla d| = 1$ and $\nabla d(x)$ is the outward pointing normal on $\mathcal{G}_{\mathrm{CT}}$. Based on this signed distance map we can define the projection $P(x) := x - d(x)\nabla d(x)$ of a point x in a neighborhood of $\mathcal{G}_{\mathrm{CT}}$ onto the closest point on $\mathcal{G}_{\mathrm{CT}}$. Thus $|P(\phi(x)) - \phi(x)|$ is a quantitative pointwise measure for the closeness of $\phi(x)$ to $\mathcal{G}_{\mathrm{CT}}$ for $x \in \mathcal{G}_r$.

Variational Formulation

Now, we are in the position to develop a suitable variational framework which allows us to cope with significantly noisy range data r_0 from the ToF camera and to simultaneously restore a reliable range function r^* and extract a suitable matching displacement u^* as a minimizer of a functional

$$\mathcal{E}[u,r] := \mathcal{E}_{\text{fid}}[r] + \kappa\mathcal{E}_{r,\text{reg}}[r] + \lambda\mathcal{E}_{\text{match}}[u,r] + \mu\mathcal{E}_{u,\text{reg}}[u]$$

consisting of a fidelity energy $\mathcal{E}_{\text{fid}}$ for the range function r given the input range function r_0, a suitable variational prior $\mathcal{E}_{r,\text{reg}}$ for the estimated range function, a matching functional $\mathcal{E}_{\text{match}}$ depending on both the range data r and the displacement u, and finally a prior $\mathcal{E}_{u,\text{reg}}$ for the displacement. Here, κ, λ, μ are positive constants which weight the contributions of the different energies.

Fidelity Energy for the Range Function. We confine here to a simple least square type functional enforcing closeness of the restored range function r to the given input data r_0 and define

$$\mathcal{E}_{\text{fid}}[r] := \int_\Omega |r - r_0|^2 \,\mathrm{d}\xi\,.$$

Let us remark that nowadays ToF devices deliver together with a dense sequence of range data frames an indicator of the reliability of the output separately for each pixel. This allows to get rid of true outliers. Denoting by $r_0^i(\xi)$ the range value at a position $\xi \in \Omega$ at time t^i and by $\chi^i(\xi)$ the corresponding reliability indicator ($\chi^i(\xi) = 1$ if $r_0^i(\xi)$ is reliable and 0 else) we actually consider time averaged input data and define at a particular time t^j the input range function r_0 of our method as $r_0^j(\xi) = \left(\sum_{i=j-m}^{i=j} \chi^i(\xi)\right)^{-1} \sum_{i=j-m}^{i=j} \chi^i(\xi) r_0^i(\xi)$ for a fixed m (in our application $m = 4$). In fact, in our model we take into account this L^2-fidelity term instead of a in general more robust L^1-functional since in the application considered here large outliers are already eliminated by this time averaging using the reliability indicator of the ToF device.

Prior for the Range Function. Range images of the thorax taken from above are characterized by steep gradients in particular at the boundary of the projected thorax surface and by pronounced contour lines. To preserve these features properly a TV-type regularization prior for the range function is decisive. On the other hand, we would like to avoid the well-known staircasing artifacts of a standard TV regularization. Hence, we take into account a pseudo Huber norm $|y|_\delta = \sqrt{|y|^2 + \delta^2}$ for $y \in \mathbb{R}^2$ and a suitably fixed regularization parameter $\delta > 0$ and define

$$\mathcal{E}_{r,\text{reg}}[r] := \int_\Omega |\nabla r|_\delta \,\mathrm{d}\xi\,.$$

Decreasing this energy comes along with a strong smoothing in flat regions which avoids staircasing and at the same time preserves large gradient magnitudes at contour lines or boundaries.

Matching Energy. The purpose of the matching functional is to ensure that $\phi(\mathcal{G}_r) \approx \mathcal{G}_{\mathrm{CT}}$ with $\phi(x) = x + u(x)$. Thus, we pick up the pointwise measure $|P(\phi(x)) - \phi(x)|$ of the mismatch at a position $x \in \mathcal{G}_r$ and obtain a first ansatz for the functional

$$\mathcal{E}_{\mathrm{match}}[u, r] := \int_{\mathcal{G}_r} |P(\phi(x)) - \phi(x)|^2 \,\mathrm{d}a = \int_{\Omega} d(\phi(X_r(\xi)))^2 \sqrt{\det DX_r(\xi)^T DX_r(\xi)} \,\mathrm{d}\xi \,.$$

Here, we have used that $|\nabla d| = 1$ and thus

$$|P(\phi(x)) - \phi(x)| = |d(\phi(x))\nabla d(\phi(x))| = |d(\phi(x))| \,.$$

The area weight $\sqrt{\det DX_r(\xi)^T DX_r(\xi)}$ with $DX_r(\xi) = Dr(\xi) \otimes \gamma(\xi) + r(\xi) D\gamma(\xi)$ involves first derivatives of r, which can be regarded as a further first order prior for the range function. We experimented with this at first glance geometrically appealing approach, but observed a strong bias between this local weight for the quality of the matching and the actual matching term $d(\phi(X_r(\xi)))^2$ leading to less accurate matching results in particular in regions of steep gradients in $r(\cdot)$ corresponding to edges or the boundary contour of $\mathcal{G}_r$.
Thus, we considered the functional

$$\mathcal{E}_{\mathrm{match}}[u, r] := \int_{\Omega} d(\phi(X_r(\xi)))^2 \,\mathrm{d}\xi = \int_{\Omega} d(r(\xi)\gamma(\xi) + u(\xi))^2 \,\mathrm{d}\xi \,.$$

This functional directly combines the range map r and the displacement u and together with the corresponding prior functions both for r and u substantiates the joined optimization approach of our method. In fact, an insufficient and possibly noisy range function r prevents a regular and suitable matching displacement and vice versa.

Prior for the Displacement. Finally, we have to take into account a regularizing prior for the displacement $u : \Omega \to \mathbb{R}^3$. Here, we consider

$$\mathcal{E}_{u,\mathrm{reg}}[u] := \int_{\Omega} |Du(\xi)|^2 \,\mathrm{d}\xi$$

with $|A|^2 := \mathrm{tr}(A^T A)$, which leads to satisfying results in our applications with a moderate rigid body motion component in the underlying deformation. Let us mention that a generalized model, which strictly incorporates rigid body motion invariance will depend on the Cauchy Green strain tensor of the deformation $\phi \circ X_r$ and thus again combines gradients of the range function r and the displacement u in a functional of the type $\int_{\Omega} W(D(\phi \circ X_r)^T(\xi) D(\phi \circ X_r)(\xi)) \,\mathrm{d}\xi$ with $D(\phi \circ X_r)(\xi) = (DX_r(\xi) + Du(\xi))$ for some energy density function W.

Joint Functional. All in all, we obtain the following joint functional

$$\mathcal{E}[u, r] = \int_{\Omega} |r - r_0|^2 + \kappa |\nabla r|_{\delta} + \lambda d(r(\xi)\gamma(\xi) + u(\xi))^2 + \mu |Du(\xi)|^2 \,\mathrm{d}\xi$$

and can postulate the following result concerning the existence of an optimal range map and a corresponding optimal deformation.

Theorem 1 (Existence of Minimizers). *Let Ω be a bounded domain, $\mathcal{G}_{\mathrm{CT}} \neq \emptyset$ and bounded, and $r_0 \in L^2(\Omega)$. Then there exists a minimizer (u^*, r^*) of $\mathcal{E}[u, r]$ on $(H^{1,2}(\Omega))^3 \times BV(\Omega)$.*

Proof. At first we observe that on a minimizing sequence the range functions are uniformly bounded in $BV(\Omega)$ because of the uniform boundedness of $\mathcal{E}_{\mathrm{fid}}$ and $\mathcal{E}_{r,\mathrm{reg}}$. From $\mathcal{G}_{\mathrm{CT}} \neq \emptyset$ we deduce that $d(\cdot)$ is Lipschitz continuous. Furthermore, $d(\cdot)$ has linear growth outside a sufficiently large ball due to the boundedness of $\mathcal{G}_{\mathrm{CT}}$. From this and the fact that the range maps are already uniformly bounded in $L^2(\Omega)$ we obtain that the displacements are uniformly bounded in $(L^2(\Omega))^3$. Taking into account the uniform bound on the displacement prior $\mathcal{E}_{u,\mathrm{reg}}$ we finally get that the displacements are uniformly bounded in $(H^{1,2}(\Omega))^3$. Hence, we can extract a subsequence for which the range functions converge weak–$*$ in $BV(\Omega)$ and the displacements converge weakly in $(H^{1,2}(\Omega))^3$. Finally, $\mathcal{E}_{\mathrm{fid}}$ and $\mathcal{E}_{\mathrm{match}}$ are continuous in r and u, $\mathcal{E}_{r,\mathrm{reg}}$ is weakly lower semicontinuous on $BV(\Omega)$, and $\mathcal{E}_{u,\mathrm{reg}}$ is convex in the Jacobian of the displacement. Thus, by the usual arguments of the direct method in the calculus of variations one verifies the existence of a minimizing range function r^* and a minimizing deformation u^*.

3 Numerical Minimization Algorithm

We consider a gradient descent method for the numerical minimization of the energy functional $\mathcal{E}[\cdot, \cdot]$, which requires the computation of the first variations with respect to the range function and the displacement, respectively. The variations of $\mathcal{E}[u, r]$ in u and r are given as

$$\partial_u \mathcal{E}[u, r](\psi) = \int_\Omega 2\lambda d(r\gamma + u)(\nabla d)(r\gamma + u) \cdot \psi + 2\mu Du : D\psi \, \mathrm{d}\xi \,,$$

$$\partial_r \mathcal{E}[u, r](\vartheta) = \int_\Omega 2(r - r_0)\vartheta + \kappa \frac{\nabla r \cdot \nabla \vartheta}{\sqrt{|\nabla r|^2 + \delta^2}} + 2\lambda d(r\gamma + u)(\nabla d)(r\gamma + u) \cdot \gamma \, \vartheta \, \mathrm{d}\xi$$

where $\vartheta : \Omega \to \mathbb{R}$ is a scalar test function and $\psi : \Omega \to \mathbb{R}^3$ is vector-valued test displacement. Furthermore, $A : B = \mathrm{tr}(A^T B)$.

For the spatial discretization a piecewise bilinear Finite Element approximation on a uniform rectangular mesh covering the image domain Ω is applied. The distance function d is precomputed using a fast marching method [16] and stored on grid nodes. In the assembly of the functional gradient we use a Gauss quadrature scheme of order 3. The total energy $\mathcal{E}$ is highly non-linear due to the involved nonlinear distance function d and the pseudo Huber norm $|\cdot|_\delta$. We take a multiscale gradient descent approach [17], solving a sequence of joint matching and denoising problems from coarse to fine scales. On each scale a non-linear conjugate gradient method is applied on the space of discrete range maps and discrete deformations. As initial data for the range function r we take

into account the raw (time averaged) range data r_0, respectively. The displacement is initialized with the zero mapping. The gradient descent is performed with respect to a regularizing metric

$$g((\delta_r, \delta_u), (\delta_r, \delta_u)) = \int_\Omega |\delta_r|^2 + \frac{\sigma^2}{2}|\nabla \delta_r|^2 + |\delta_u|^2 + \frac{\sigma^2}{2}|D\delta_u|^2$$

where δ_r and δ_u are increments in the range function r and the displacement u, respectively. Furthermore, σ corresponds to a Gaussian type filter width acting on the descent directions. As time step control the Armijo rule is taken into account [18]. We stop iterating as soon as the energy decay is sufficiently small.

4 Validation and Application of the Model

To validate our model we have investigated the validation on a real CT and synthetic ToF data (rigid torso phantom), on synthetic CT and ToF data (NCAT respiration phantom), and finally the application to a real CT and real ToF data (rigid torso phantom).

Underlying Data. CT data was acquired on a Siemens SOMATOM Sensation 64 for a male torso phantom at a resolution of $512 \times 512 \times 346$ voxels with a spacing of $0.95 \times 0.95 \times 2.50\,\mathrm{mm}^3$. The surface $\mathcal{G}_{\mathrm{CT}}$ with an approximate diameter of 33 cm is extracted from this data set using a thresholding based region growing segmentation, a marching cube algorithm on the resulting binary segmentation mask followed by a Laplacian mesh smoothing. ToF frame sequences were acquired using a CamCube 3.0 ToF camera from PMD Technologies GmbH[1] with a resolution of 200×200 pixels, a frame rate of 40 Hz, a modulation frequency of 20 MHz, an infrared wavelength centered at 870 nm, an integration time of 750 μs, and a lens with $40° \times 40°$ field of view. This frame rate renders a temporal averaging over 5 frames as acceptable. At the clinical working distance of 1-1.5 m, the noise level of the range measurements is $\sigma^2 \approx 40\,\mathrm{mm}^2$. In addition we have used the NCAT: 4D NURBS-based CArdiac-Torso phantom [19] and generated (artificial) CT data for 16 states within one respiration cycle. For each state, the phantom surface mesh is extracted with the segmentation and mesh generation pipeline sketched above (voxel spacing (x,y,z): $3.125 \times 3.125 \times 3.125\,\mathrm{mm}^3$ and overall resolution of $256 \times 256 \times 191$ voxels). The length of the underlying respiratory cycle is 5 s with an extent of diaphragm motion of 20 mm, an extent of the AP chest expansion of 12 mm (respiration start phase: full exhale, full inhale: 0.4). We generated a typical RT treatment scene by adding a treatment table plane. The synthetic data generation follows the proposal in [20] but has been simplified: Instead of simulating the photon mixing device we directly operate on simulated distance values based on the z-buffer representation of a 3D scene. We then approximate the temporal noise on a per-pixel basis by adding an individual offset drawn from a standard normal with $\sigma^2 = 40\,\mathrm{mm}^2$. This

[1] http://www.pmdtec.com/

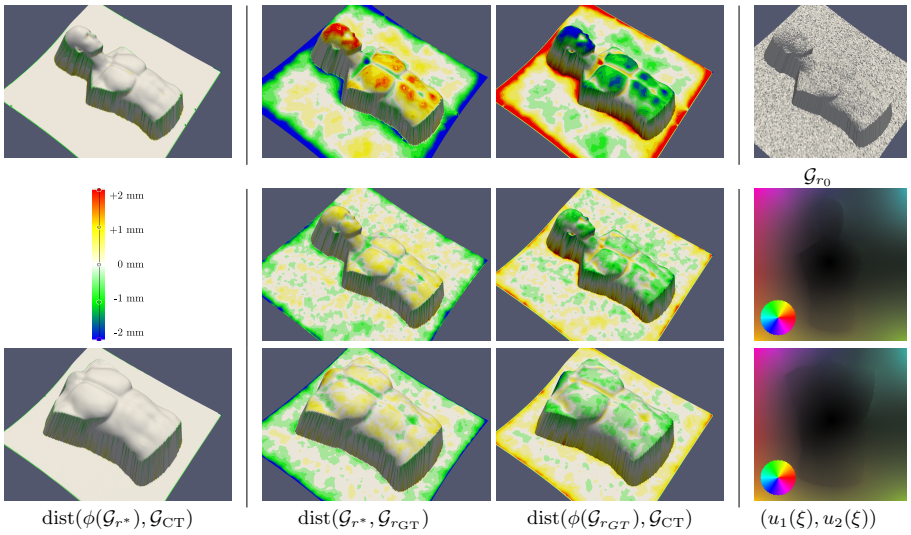

Fig. 2. Validation of the model on a male phantom $\mathcal{G}_{\mathrm{CT}}$ (top left and bottom left). The first two lines correspond to results for the full torso incl. head, whereas the third line refers to results for the thorax and abdomen part of the phantom. As quantitative measure of the denoising and registration results we show the distance $\mathrm{dist}(\mathcal{G}_{r^*}, \mathcal{G}_{r_{\mathrm{GT}}})$ on $\mathcal{G}_{r^*}$ (middle left) and the distance $\mathrm{dist}(\phi(\mathcal{G}_{r_{GT}}), \mathcal{G}_{\mathrm{CT}})$ on $\phi(\mathcal{G}_{r_{GT}})$ (middle right) color coded from $-2\,\mathrm{mm}$ to $+2\,\mathrm{mm}$ using the color bar on the left. Results in the first row correspond to raw, non time averaged range data, whereas in the second and third row a time averaging with $m = 4$ is taken into account. Furthermore, $\mathcal{G}_{r_0}$ for time averaged range data r_0 is shown (top right) and a color coding of the resulting in plane displacement is rendered below for the full torso incl. head (second row) and the sole torso (third row) in case of the time averaged range data (angle and length of the vector $(u_1(\xi), u_2(\xi))$ are encoded as color and brightness, respectively).

variance is motivated by observations on real ToF data at the clinical working distance of about 1-1.5 m. As rather large synthetic deformation we have taken into account $u_{1/2}(x) = \alpha(\pm x_1(x_2 - 1/2) + (1 - x_1)(x_1 - 1/2))$ and $u_3(x) = 0$ with a comparably large deformation scale parameter $\alpha = 0.1$.

Algorithmic Validation Setup. The workflow of the preparatory phase of our validation experiments is as follows: At first we load the torso mesh (real CT phantom or NCAT). Next, we generate a ground truth range image r_{GT}. Then, we generate a synthetic ToF image by adding Gaussian noise with a particular standard derivation σ: $r_{\mathrm{noisy}} = r_{\mathrm{GT}} + \mathrm{noise}_{\sigma^2}$. Furthermore, we deform the phantom torso by the synthetic deformation (in the 2D table plane) to generate a planning CT surface $\mathcal{G}_{\mathrm{CT}}^{\mathrm{phantom}}$. Finally, we generate the discrete signed distance function from the triangular planning CT surface on a 3D mesh of grid resolution 257^3.

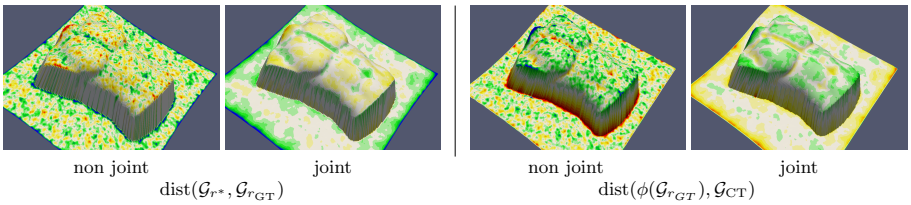

Fig. 3. Comparison of denoising and subsequent registration to the proposed joint approach for time averaged range data r_0. The two left images show $\mathrm{dist}(\mathcal{G}_{r^*}, \mathcal{G}_{r_{\mathrm{GT}}})$ on $\mathcal{G}_{r^*}$ for the non joint (left) and joint approach (right). The two right images depict the distance measure $\mathrm{dist}(\phi(\mathcal{G}_{r_{GT}}), \mathcal{G}_{\mathrm{CT}})$ on $\phi(\mathcal{G}_{r_{GT}})$ for the non joint (left) and joint approach (right). The color coding is the same as in Fig. 2.

Validation Results for the Real CT and Synthetic Range Data. In Fig. 2, results of our algorithm are shown for a phantom torso and artificially generated range data. We compare the case of unfiltered range data with a suitable set of model parameters ($\kappa = 0.0004$, $\lambda = 10000$, $\mu = 0.004$) to the case of time averaged range data with an adapted set of parameters ($\kappa = 0.0001$, $\lambda = 2500$, $\mu = 0.001$). In addition, we evaluate the benefits of the joint approach in comparison to an algorithm, where one first denoises r_0 and then computes a matching of $\mathcal{G}_r$ and $\mathcal{G}_{\mathrm{CT}}$. Fig. 3 shows that the joint approach is superior to the subsequent denoising and registration approach. Obviously, incorporating prior knowledge about the target shape $\mathcal{G}_{\mathrm{CT}}$ helps substantially in the denoising process. On the other hand, proper denoising also renders the registration problem more robust. Furthermore, we study the impact of different denoising models in Fig. 4, where the proposed regularization using the pseudo Huber norm is compared to a simple quadratic regularization energy $\kappa \int_\Omega |\nabla r|^2$ and an egde preserving TV regularization of r. The oversmoothing effect of the quadratic model and the staircasing artifacts of the TV model are clearly visible. Here, time averaged ToF data has been investigated and $\kappa = 0.0001$.

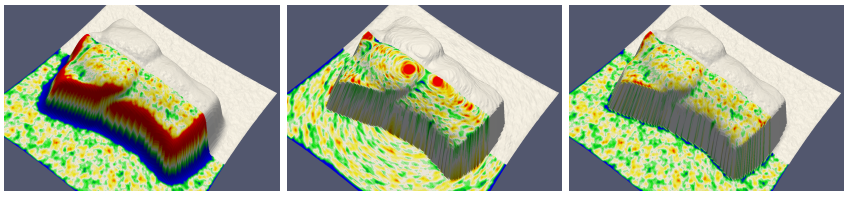

Fig. 4. An experimental evaluation of different denoising models is performed. From left to right the distance $\mathrm{dist}(\mathcal{G}_{r^*}, \mathcal{G}_{r_{\mathrm{GT}}})$ is color coded on $\mathcal{G}_{r^*}$ for a quadratic regularization, a TV regularization, and the proposed regularization via the pseudo Huber norm of ∇r. The color coding is the same as in Fig. 2.

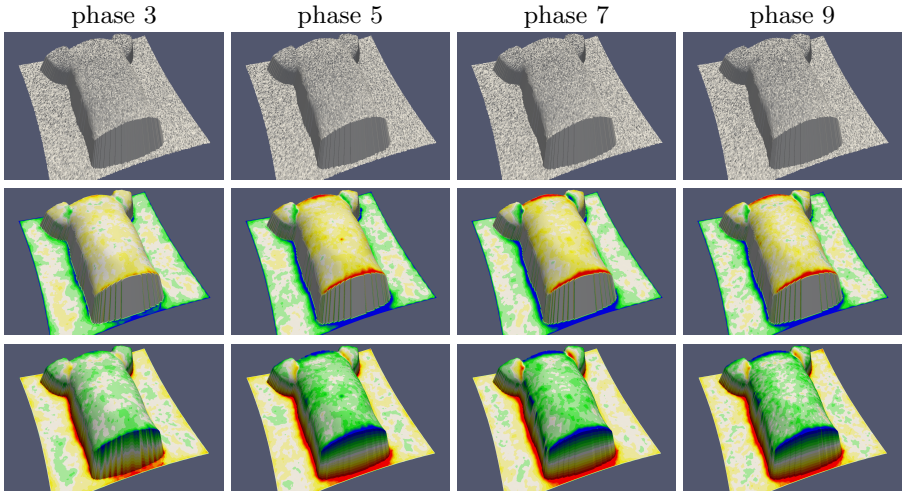

Fig. 5. Four different phases of a respiration cycle $\mathcal{G}_{r_0}$ for time averaged range data r_0 are depicted (first row). The distance $\mathrm{dist}(\mathcal{G}_{r^*}, \mathcal{G}_{r_{\mathrm{GT}}})$ on $\mathcal{G}_{r^*}$ (second row) and the distance $\mathrm{dist}(\phi(\mathcal{G}_{r_{GT}}), \mathcal{G}_{\mathrm{CT}})$ on $\phi(\mathcal{G}_{r_{GT}})$ (third row) are color-coded as in Fig. 2.

Application Benchmark for a 4D CT Respiration Phantom. In Fig. 5, we consider the joint denoising and registration of the synthetic ToF data ($\sigma^2 = 40mm^2$, time averaging over 5 frames) based on the 4D CT respiration phantom with 16 phases. Thereby, the phantom volume at full expiration is considered as the CT geometry $\mathcal{G}_{\mathrm{CT}}$ (phase 1 out of 16). To speed up the algorithm we now take into account the estimated deformation field and the denoised range data from the previous phase as initial data for our algorithm on the next phase. Table 1 compares this to an initialization of r with r_0 and u with the zero displacement. We observe a reduction of the required gradient descent steps by a factor $\frac{1}{3}$ without any change of the resulting minimal energy. Here, the model parameters are $\kappa = 0.0001$, $\lambda = 2500$, $\mu = 0.001$.

Application to Real CT and Real ToF Data. Finally, we study the performance of our algorithm on real CT and real ToF data based on the rigid torso phantom

Table 1. The number of non-linear CG steps are reported for different phases of a respiration cycle for our method with and without initialization based on the previously processed respiration phase.

respiration phases	phase 3		phase 5		phase 7		phase 9	
	# it	$\mathcal{E}[u^*, r^*]$	# it	$\mathcal{E}[u^*, r^*]$	# it	$\mathcal{E}[u^*, r^*]$	# it	$\mathcal{E}[u^*, r^*]$
No initial.	1743	1.778	1602	1.818	1781	1.832	1812	1.832
incremental initial.	662	1.778	418	1.818	538	1.832	470	1.832

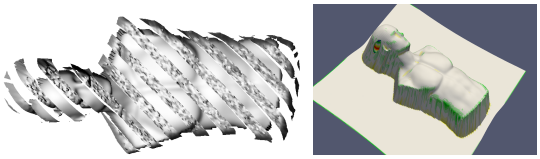

Fig. 6. On the left $\mathcal{G}_{r_0}$ for time averaged real ToF data and the underlying CT phantom $\mathcal{G}_{\mathrm{CT}}$ are rendered in a single image using alternating slices. On the right the distance $\mathrm{dist}(\phi(\mathcal{G}_{r^*}), \mathcal{G}_{\mathrm{CT}})$ on $\phi(\mathcal{G}_{r^*})$ is again color-coded as in Fig. 2.

in Fig. 6. Here, we apply a time averaging of the range data over 5 frames and use the parameters $\kappa = 0.0001$, $\lambda = 2500$, and $\mu = 0.001$. We observe that even topological artifacts (systematical errors of the ToF data due to intensity related distance errors) can be removed and we obtain satisfying denoising and matching results using the proposed joint denoising and registration approach.

5 Discussion and Conclusion

We have proposed a joint variational model for the denoising of ToF range data and the simultaneous matching with a surface extracted from CT data. The approach turned out to be of strong potential for the application in radiation therapy, where respiratory motion has to be compensated to improve therapy planning and treatment. The joint approach is capable of significantly reducing systematic errors from ToF imaging and the obtained quantitative results are within the intended tolerance margins. Based on this approach in a next step a reliable 3D extension of the matching displacement onto the whole geometric model can be computed, which would then finally allow an adaptive steering of the beam in the radiation therapy.

Acknowledgments S. Bauer gratefully acknowledges the support by the European Union (Europäischer Fonds für regionale Entwicklung) and the Bayerisches Staatsministerium für Wirtschaft, Infrastruktur, Verkehr und Technologie (StMWIVT), in the context of the R&D program IUK Bayern under Grant No. IUK338/001.

References

1. Keall, P.J., Mageras, G.S., Balter, J.M., Emery, R.S., Forster, K.M., Jiang, S.B., Kapatoes, J.M., Low, D.A., Murphy, M.J., Murray, B.R., Ramsey, C.R., Herk, M.B.V., Vedam, S.S., Wong, J.W., Yorke, E.: The management of respiratory motion in radiation oncology, report of AAPM task group 76. Med Phys **33**(10) (2006) 3874–3900

2. Essapen, S., Knowles, C., Norman, A., Tait, D.: Accuracy of set-up of thoracic radiotherapy: prospective analysis of 24 patients treated with radiotherapy for lung cancer. Br J Radiol **75**(890) (2002) 162–169
3. Johnson, U., Landau, D., Lindgren-Turner, J., Smith, N., Meir, I., Howe, R., Rodgers, H., Davit, S., Deehan, C.: Real time 3D surface imaging for the analysis of respiratory motion during radiotherapy. International Journal of Radiation Oncology Biology Physics **60**(Supplement 1) (2004) 603–604
4. Schaller, C., Penne, J., Hornegger, J.: Time-of-Flight Sensor for Respiratory Motion Gating. Medical Physics **35**(7) (2008) 3090–3093
5. Fayad, H., Pan, T., Roux, C., Le Rest, C., Pradier, O., Clement, J., Visvikis, D.: A patient specific respiratory model based on 4D CT data and a time of flight camera (TOF). In: Proceedings of IEEE NSS/MIC. (2009) 2594–2598
6. Fayad, H., Pan, T., Roux, C., Le Rest, C., Pradier, O., Visvikis, D.: A 2D-spline patient specific model for use in radiation therapy. In: Proceedings of IEEE ISBI. (2009) 590 –593
7. McClelland, J., Blackall, J., Tarte, S., Chandler, A., Hughes, S., Ahmad, S., Landau, D., Hawkes, D.: A continuous 4D motion model from multiple respiratory cycles for use in lung radiotherapy. Medical Physics **33**(9) (2006) 3348–3358
8. Kolb, A., Barth, E., Koch, R., Larsen, R.: Time-of-flight sensors in computer graphics. In: Proceedings of Eurographics. (2009) 119–134
9. Schaller, C., Adelt, A., Penne, J., Hornegger, J.: Time-of-flight sensor for patient positioning. In Samei, E., Hsieh, J., eds.: Proceedings of SPIE Medical Imaging. Volume 7258. (2009) 726110
10. Lindner, M., Schiller, I., Kolb, A., Koch, R.: Time-of-flight sensor calibration for accurate range sensing. Computer Vision and Image Understanding **114**(12) (2010) 1318 – 1328 Special issue on Time-of-Flight Camera Based Computer Vision.
11. Kapur, T., Yezzi, L., Zöllei, L.: A variational framework for joint segmentation and registration. In: Proceedings of IEEE Workshop on Mathematical Methods in Biomedical Image Analysis. (2001) 44–51
12. Unal, G., Slabaugh, G., Yezzi, A., Tyan, J.: Joint segmentation and non-rigid registration without shape priors. Technical Report SCR-04-TR-7495, Siemens Corporate Research (2004)
13. Féron, O., Mohammad-Djafari, A.: Image fusion and unsupervised joint segmentation using a HMM and MCMC algorithms. J. of Electronic Imaging **15**(02) (2004) 023014
14. Droske, M., Rumpf, M.: Multi scale joint segmentation and registration of image morphology. IEEE Transaction on Pattern Recognition and Machine Intelligence **29**(12) (2007) 2181–2194
15. Buades, T., Lou, Y., Morel, J., Tang, Z.: A note on multi-image denoising. In: Proceedings of International Workshop on Local and Non-Local Approximation in Image Processing. (2009) 1–15
16. Russo, G., Smereka, P.: A remark on computing distance functions. Journal of Computational Physics **163** (2000) 51–67
17. Alvarez, L., Weickert, J., Sánchez, J.: A scale–space approach to nonlocal optical flow calculations. In Nielsen, M., Johansen, P., Olsen, O.F., Weickert, J., eds.: Proceedings of International Conference on Scale-Space Theories in Computer Vision. LNCS; 1682, Springer (1999) 235–246
18. Armijo, L.: Minimization of functions having Lipschitz continuous first partial derivatives. Pacific Journal of Mathematics **16**(1) (1966) 1–3

19. Segars, W., Mori, S., Chen, G., Tsui, B.: Modeling respiratory motion variations in the 4D NCAT phantom. In: Proceedings of IEEE NSS/MIC. Volume 4. (2007) 2677–2679
20. Keller, M., Orthmann, J., Kolb, A., Peters, V.: A simulation framework for time-of-flight sensors. In: Proceedings of ISSCS. (2007) 1–4